Little Red Dots as the Very First Activity of Black Hole Growth

Kohei Inayoshi [ORCID]
Kavli Institute for Astronomy and Astrophysics, Peking University, Beijing 100871, People's Republic of China; inayoshi@pku.edu.cn

Abstract

The James Webb Space Telescope has detected massive black holes (BHs) with masses of $\sim 10^{6-8}\,M_\odot$ within the first billion years of the Universe. One of the remarkable findings is the identification of "little red dots" (LRDs), a unique class of active galactic nuclei (AGNs) with distinct characteristics representing a key phase in the formation and growth of early BHs. Here, we analyze the occurrence rate of LRDs, which emerge around redshifts $z \sim 6$–8 and sharply decline at $z < 4$. We find that this trend follows a log-normal distribution, commonly observed in phenomena driven by stochastic and random factors. We propose a hypothesis that the first one or two AGN events associated with newly formed seed BHs are observed as LRDs, and their unique features fade in the subsequent episodes. This naturally explains the cosmic evolution of AGN abundance over $0 < z < 5$, which follows $\propto (1 + z)^{-5/2}$ due to the cumulative effect of recurring AGN activity. The unique characteristics of LRDs are likely linked to the dense gas environments around the seed BHs, which create strong absorption features in the broad-line emission and enable super-Eddington accretion bursts, ultimately yielding the observed overmassive nature of BHs compared to the local relationship. An analytical expression for the redshift evolution of LRD abundance is provided for direct comparison with future observational constraints.

Unified Astronomy Thesaurus concepts: Galaxy formation (595); High-redshift galaxies (734); Quasars (1319); Supermassive black holes (1663)

1. Introduction

The James Webb Space Telescope (JWST) has revolutionized extragalactic research, uncovering low-luminosity active galactic nuclei (AGNs) at high redshifts of $z > 4$–7 powered by accreting black holes (BHs) with masses of $\sim 10^{6-8}\,M_\odot$ (e.g., Y. Harikane et al. 2023; D. D. Kocevski et al. 2023; M. Onoue et al. 2023; R. Maiolino et al. 2024; A. J. Taylor et al. 2025a). Among these ground-breaking discoveries, the identification of "little red dots" (LRDs) stands out as particularly remarkable. LRDs are extremely compact objects (<100 pc) characterized by broad emission lines on red continuum spectra, indicating the presence of dust-obscured AGNs (e.g., J. E. Greene et al. 2024; J. Matthee et al. 2024; I. Labbe et al. 2025). Their cosmic abundance is several orders of magnitude higher than that of bright quasars, allowing them to be detectable even within JWST's narrow field of view (H. B. Akins et al. 2024; V. Kokorev et al. 2024a; D. D. Kocevski et al. 2025). Under standard assumptions in measurement, these objects show BH-to-galaxy mass ratios far above the empirical values observed in the nearby Universe (e.g., J. Kormendy & L. C. Ho 2013; A. E. Reines & M. Volonteri 2015), suggesting that they preserve crucial information on the formation of seed BHs and their early rapid growth phases.

Despite their significance, key questions about the spectral nature of LRDs arise from multiwavelength observations (e.g., J. E. Greene et al. 2024; I. Juodžbalis et al. 2024; P. G. Pérez-González et al. 2024; B. Wang et al. 2024, 2025; D. D. Kocevski et al. 2025; R. Maiolino et al. 2025): (1) the prominent absorption feature in broad Balmer emission lines, (2) the deficit of hot dust emission, (3) the "v-shape" spectral energy distribution in the rest-frame UV-optical range, and (4) the absence of X-ray detections. These characteristics indicate that LRDs might represent a unique phase of AGN activity in their formation, and a potential contribution from super-Eddington accretion (K. Inayoshi et al. 2020; M. Volonteri et al. 2021, and references therein).

Throughout this paper, we assume a flat Λ cold dark matter (CDM) cosmology consistent with the constraints from Planck (Planck Collaboration et al. 2016); $h = 0.677$, $\Omega_{\rm m} = 0.307$, $\Omega_\Lambda = 1 - \Omega_{\rm m}$, and $\Omega_{\rm b} = 0.0486$.

2. Cosmic Evolution of LRD Numbers

To date, more than 300 LRDs have been identified through JWST survey programs, using photometric color selection techniques. We adopt a sample of 341 LRDs spanning over $z \sim 2$–11, compiled from the CEERS, PRIMER, JADES, UNCOVER, and NGDEEP surveys (D. D. Kocevski et al. 2025). These LRDs were selected using a spectral slope fitting technique, which employs shifting bandpasses to sample the same rest-frame emission both blueward and redward of the 4000 Å break, and enables a self-consistent search for AGN candidates with red optical and blue UV colors over a wide range of redshifts (see also K. N. Hainline et al. 2025).

In the left panel of Figure 1, we present the occurrence rate of the LRD sample as a function of cosmic time (bottom x-axis) and redshift (top x-axis). The histogram shows 341 photometrically selected LRDs (blue), including 39 with spectroscopically confirmed redshift. The colored bars indicate the redshift range where the 4000 Å break falls within the bandpass of each wide-band filter. These LRDs with unique v-shape spectra and compact morphology emerge at $z \sim 8$, but the number begins to decline at $z \lesssim 6$, and experience a rapid drop at $z \sim 4$ (D. D. Kocevski et al. 2025). For $z > 8$, the turnover wavelength enters the F356W band, while red optical continua are observed only in F444W (and F410M, if available). As a result, the selection of $z > 9$ LRDs becomes
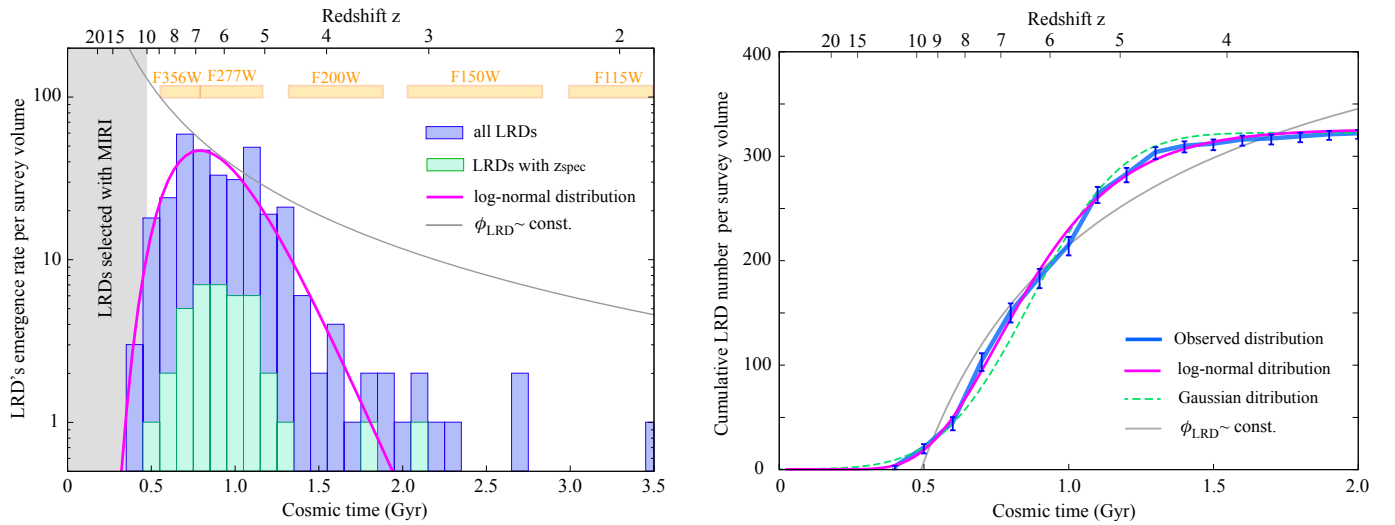
Figure 1. Left: the occurrence rate of LRDs as a function of cosmic time (bottom x-axis) and redshift (top x-axis). The histogram, based on the data from D. D. Kocevski et al. (2025), shows 341 photometrically selected LRDs (blue), including 39 with spectroscopically confirmed redshifts (green). The colored bars indicate the redshift range where the 4000 Å break falls within the bandpass of each wide-band filter. The photometric selection of $z > 9$ LRDs becomes incomplete (gray shaded region). The magenta curve represents the best-fit function with a log-normal distribution, while the gray curve shows the case with constant abundance in unit comoving volume for reference. Right: the cumulative number distribution of the observed LRD number (blue) with error bars computed via binomial statistics. The best-fit result obtained using a log-normal distribution is shown ($p = 0.873$), along with a Gaussian distribution yielding a worse fit ($p = 1.17 \times 10^{-4}$).

incomplete, and thus the number might drop toward higher redshifts.[1] On the low-redshift side ($z < 4$), the number of LRD detections rapidly decreases, even though the available NIRCam bands are capable of capturing the 4000 Å break. It is worth noting that the histogram distributions of the total LRD sample and the subset with spectroscopic redshifts show similar shapes without significant skewness. This suggests that photometric redshift measurements provide a reliable estimate of their true values for these LRD samples. For comparison, we consider a scenario where the comoving number density of LRDs remains constant over time, yielding a reference evolution for the occurrence rate: $dN/dt = \phi \cdot (dV_c/dz)(dz/dt) \propto t^{-5/3}$, or equivalently $\propto (1 + z)^{5/2}$ (gray curve). The observed decline in the LRD occurrence rate, however, deviates significantly from the reference evolution.

This implies that LRD activity is not a process that repeats continuously over cosmic time, but instead occurs sporadically due to complex and random factors. In many natural systems (e.g., earthquakes and astronomical phenomena such as gamma-ray bursts and fast radio bursts), the waiting time between successive events follows a log-normal distribution (e.g., H. Li & E. E. Fenimore 1996; W. L. Ellsworth et al. 1999; F. Kirsten et al. 2024), reflecting the stochastic nature of these events. Inspired by these analogies, we employ the standard chi-square minimization technique to fit the observed data with errors estimated from Poisson statistics, using a log-normal distribution defined as

$$\frac{dN}{dt} = \frac{N_0}{\sqrt{2\pi}\,\sigma_0 t} \exp\left[-\frac{\{\ln(t/t_0)\}^2}{2\sigma_0^2}\right]. \quad (1)$$

From the fitting procedure, we find the best-fit parameters (reduced chi-square $\chi_\nu^2 = 2.02$): $t_0 = 865 \pm 22$ Myr and $\sigma_0 = 0.297 \pm 0.0184$ with a time bin of $\Delta t = 100$ Myr

(magenta curve). Importantly, the log-normal fit remains robust even when the histogram is restricted to LRDs with UV absolute magnitudes, $M_{UV} < -18$ mag, where detection is not significantly affected by flux limits. This strengthens the validity of our argument, indicating that the observed trend is intrinsic to LRDs rather than a selection effect (see more details in Appendix A).

The right panel of Figure 1 shows the cumulative number distribution of LRDs. For $t > 1.3$ Gyr, the distribution flattens due to the sharp decline in the number of sources. For comparison, we overlay three curves representing different fitted distribution functions for the occurrence rate: a log-normal distribution (magenta), a Gaussian distribution (green), and a power-law form with $dN/dt \propto t^{-5/3}$ (gray), which assumes a constant ϕ_{LRD}. The log-normal distribution provides our best-fit model ($\chi_\nu^2 = 0.647$ and $p = 0.873$) with $t_0 = 837 \pm 6$ Myr and $\sigma_0 = 0.327 \pm 0.00803$. These values are in good agreement with the previous fitting results for the occurrence rate.[2] The Gaussian model yields a slightly worse fit ($\chi_\nu^2 = 2.65$ and $p = 1.17 \times 10^{-4}$), as the function form fails to capture the asymmetric feature of the distribution. The low p-value ($\ll 1$) indicates that the Gaussian model is statistically inconsistent with the observed data. The power-law model does not explain the flattening of the cumulative distribution ($\chi_\nu^2 = 13.6$). Even when the power-law index is treated as a free parameter, the best-fitting function ($dN/dt \propto t^{-2.85}$) still does not match the observed trend well. Such a steep decline cannot be only attributed to the loss of LRD features, particularly their compact morphology, due to mergers with normal galaxies (see Appendix B), though mergers may play a partial role in their disappearance (K. Inayoshi et al. 2025; F. M. Khan et al. 2025).

Assuming a log-normal form for the occurrence rate given in Equation (1), the cosmic evolution of LRDs is described by

---

[1] Recently, a $z \sim 9$ LRD candidate has been spectroscopically confirmed as a broad-line (Hβ) AGN at $z_{spec} = 9.288$ (CAPERS-LRD-z9; A. J. Taylor et al. 2025b). This object will be an anchor point to test the log-normal distribution hypothesis.

[2] Although the fitting result generally depends on the choice of time bin, the consistency of the fitted parameters based on the differential and cumulative distribution functions ensures the robustness of the fitting result.

the following expression:

$$\phi_{\mathrm{LRD}} = \phi_0 f(z) \exp\left[-\frac{\{\ln(1+z) - \mu_z\}^2}{2\sigma_z^2}\right], \qquad (2)$$

where $\log(\phi_0/\mathrm{Mpc}^{-3}) = -5.2762 \pm 0.0015$, $\mu_z = \ln(1 + z_0)$ with a characteristic redshift of $z_0(=6.53^{+0.04}_{-0.03})$ corresponding to the cosmic age $t_0(= 837 \pm 6\,\mathrm{Myr})$, and $\sigma_z = 2\sigma_0/3(= 0.218 \pm 0.00535)$. Here, the cosmic age is converted to redshift using $t \simeq 2/(3H_0\sqrt{\Omega_{\mathrm{m}}})(1+z)^{-3/2}$, which holds for $z \gg (\Omega_\Lambda/\Omega_{\mathrm{m}})^{1/3} - 1 \simeq 0.3$. The function $f(z)$ accounts for the redshift dependence of both the comoving volume element per redshift bin dV_{c}/dz, and the cosmic time interval dt/dz, and is well approximated with the analytical form

$$f(z) = \frac{(1+z)^{3/2}}{[s(1+z)^{1/2} - 1]^2}, \qquad (3)$$

and $s = 0.903$ is fitted for a flat ΛCDM Universe with $\Omega_{\mathrm{m}} = 0.307$ at $z \geqslant 1.5$.[3] These formulae in Equations (2) and (3) with three parameters (ϕ_0, μ_z, and σ_z) provide an effective modeling for the abundance and redshift evolution of LRDs as new observational constraints become available, particularly at lower redshifts (see Y. Ma et al. 2025). This analytical form can also be applied to study the redshift evolution of LRD luminosity functions within individual magnitude bins.

3. Discussion

Based on our finding that the occurrence rate of LRDs follows a log-normal distribution, we propose a hypothesis for the origin of LRDs: the first one or two AGN events associated with a newly formed seed BH are observed as LRDs due to the unique characteristics of the surrounding environment. After these initial accretion episodes, the LRD features fade, and the objects transition into normal AGNs.

In this scenario, LRDs represent the earliest phase of AGN activity from newly born BH seeds with $\sim 10^{4-5}\,M_\odot$, which are likely embedded in dense gas environments (e.g., V. Bromm & A. Loeb 2003; M. C. Begelman et al. 2006; C. Shang et al. 2010) with abundances of $\sim 10^{-5}$–$10^{-4}\,\mathrm{Mpc}^{-3}$, corresponding to those of atomic-cooling halos in overdense regions where intense Lyman–Werner radiation and/or violent halo mergers enhance the possibility of BH seeding through suppression of H_2 formation and cooling (e.g., R. Valiante et al. 2016; W. Li et al. 2021; A. Trinca et al. 2022; W. Li et al. 2023). This dense gas leads to strong absorption features on top of the broad Balmer emission lines, which is one of the key spectral signatures for LRDs (I. Juodžbalis et al. 2024; J. Matthee et al. 2024; X. Ji et al. 2025). Furthermore, if the gas surrounding the seed BH accretes at super-Eddington rates, this would naturally explain the observed X-ray weakness and weak (but observable) variability of LRDs (K. Inayoshi et al. 2024; P. Madau & F. Haardt 2024). When the BH grows rapidly at a rate with an Eddington ratio of $\lambda_{\mathrm{Edd}} \sim O(10)$, the e-folding time of BH growth is $t_{\mathrm{grow}} \simeq 1.5\,\mathrm{Myr}\,(\lambda_{\mathrm{Edd}}/30)^{-1}$. This implies that the seed BH can reach a mass of $10^7\,M_\odot$

within just one or two accretion episodes, each lasting several Myr (e.g., K. Inayoshi et al. 2022). Once the BHs grow in mass substantially, super-Eddington accretion becomes unsustainable due to a reduced mass supply from the galaxy environment (H. Hu et al. 2022; M. T. Scoggins & Z. Haiman 2024; H. Hu et al. 2025). As a result, the BHs transition from the early super-Eddington accretion phase to a more typical AGN phase, after making the BHs largely overmassive compared to the BH-to-galaxy mass ratio measured in the nearby Universe (e.g., Y. Harikane et al. 2023; R. Maiolino et al. 2024; C.-H. Chen et al. 2025; D. D. Kocevski et al. 2025; A. J. Taylor et al. 2025b).

Assuming the physical processes driving both LRDs and normal AGNs are essentially the same, and the time interval between each individual event follows a similar statistical distribution, the cosmic evolution of AGN abundances should evolve in a similar fashion for LRDs. However, observations reveal that while LRDs show a rapid decline in occurrence rate, the occurrence rate of normal AGNs remains nearly constant down to low redshifts (I. Delvecchio et al. 2014; Y. Ueda et al. 2014; E. Pouliasis et al. 2024). This discrepancy suggests that factors beyond the timing of single events (for instance, the recurrence of AGN activity) play a role in shaping the cosmic evolution of the bulk AGN population.

To investigate this, we model the occurrence times of AGN events as independently and identically distributed, making two key assumptions: (1) the occurrence time follows a single distribution in each episode, and (2) the occurrence time for each individual AGN is independent of others, with no direct influence on the timing of subsequent events. Under these assumptions, we generate a set of independent random variables t_i, drawn from a log-normal distribution to represent individual AGN occurrence times. We then compute the probability distribution of the total elapsed time across multiple episodes, defined as the sum of n independent log-normal variables, $T_n = \sum_{i=1}^{n} t_i$. To obtain a statistically robust distribution, we perform Monte Carlo sampling for each T_n and numerically construct its probability distribution. Note that as $n \to \infty$, the distribution of T_n approaches a Gaussian distribution according to the central limit theorem, allowing for an analytical treatment for this calculation (see Appendix C).

In the left panel of Figure 2, each curve presents the AGN population categorized by the number of active episodes that the nuclear BH undergo, showing the distribution of T_n: the first ($n = 1$; magenta), second ($n = 2$; green), third ($n = 3$; cyan), and fourth ($n = 4$; orange) episodes, as well as the total population, which includes up to eight episodes ($n = 8$; black). The normalization of the modeled abundance is set such that the number of objects in their first active episodes matches the observed abundance of LRDs at $z \sim 4$–7, which is $\phi_{\mathrm{LRD}} \simeq (2\text{–}5) \times 10^{-5}\,\mathrm{Mpc}^{-3}$ integrated over $-20 \leqslant M_{\mathrm{UV}}/\mathrm{mag} \leqslant -18$ (V. Kokorev et al. 2024a; D. D. Kocevski et al. 2025). Since the total number of objects is conserved across successive episodes, the modeled AGN abundance at $z < 5$ is not explicitly fitted to the observational data. Nevertheless, the predicted abundance from this log-normal model agrees well with observations of LRD candidates at lower redshifts, photometrically selected by wide-area ground-based telescope surveys (Y. Ma et al. 2025), as well as with X-ray-selected AGNs over $0 < z < 5$ (Y. Ueda et al. 2014) and $4 < z < 6$ (E. Pouliasis et al. 2024). As the LRD number decreases at $z < 4$, the total AGN abundance

---

[3] The functional form in Equation (3) is motivated by the integral form of $\int_0^z dz'/\sqrt{\Omega_{\mathrm{m}}(1 + z')^3 + \Omega_\Lambda}$ in the matter-dominant Universe. The parameter s is determined by the integral contribution from the low-redshift Universe. For $\Omega_{\mathrm{m}} = 0.3$, a value commonly adopted in observational studies, we obtain $s = 0.90066$.
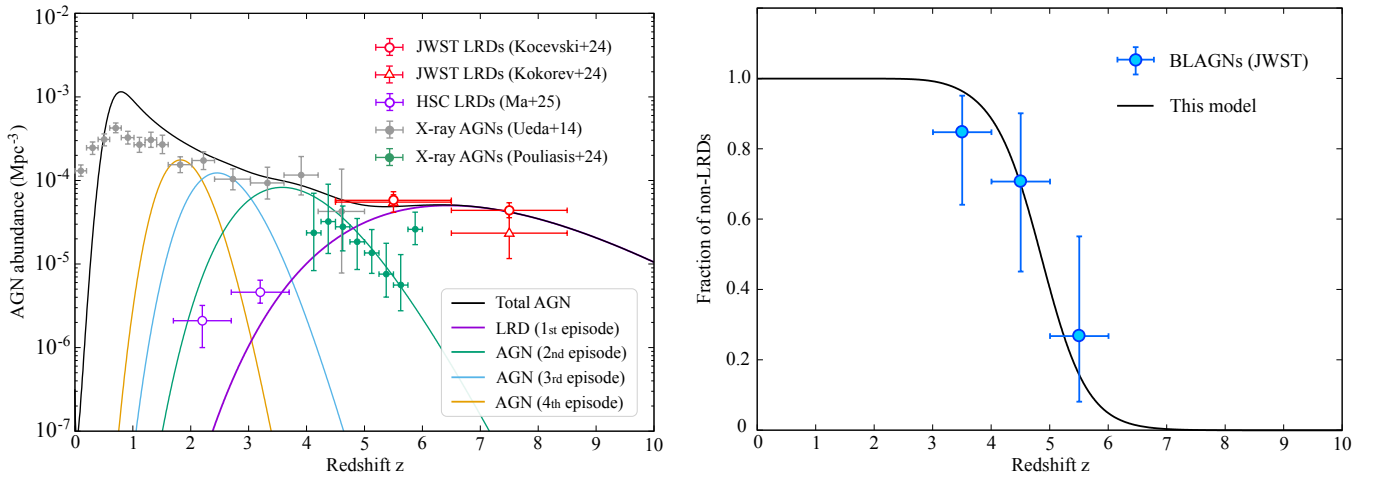
Figure 2. Left: the redshift dependence of the AGN comoving number density. Each modeled curve presents the AGN population that undergo nth AGN active episodes, illustrating the distribution of the total elapsed time T_n ($1 \leqslant n \leqslant 8$): the first (magenta), second (green), third (cyan), and fourth (orange) episodes, as well as the total population in this model (black). The normalization is set such that the modeled LRD abundance is consistent with the observed ones (red; V. Kokorev et al. 2024a; D. D. Kocevski et al. 2025). The predicted abundance in this model agrees with those of LRD candidates at $1.7 < z < 3.7$ photometrically selected by wide-area ground-based telescope surveys (purple; Y. Ma et al. 2025), as well as with X-ray selected AGNs over $0 < z < 5$ (gray; Y. Ueda et al. 2014) and $4 < z < 6$ (green; E. Pouliasis et al. 2024). Right: the fraction of non-LRDs (black curve; model) and observational constraints on the fraction (95% confidence level) derived from a sample of 62 broad-line AGNs (blue symbol; A. J. Taylor et al. 2025a).

curve increases toward lower redshifts, reflecting the shift from LRDs to more typical AGN populations. This trend is consistent with our finding of $\phi \propto (1 + z)^{-5/2}$, which is derived from the nearly constant occurrence rate of AGN activity (see Equation (C2)). Moreover, the rapid emergence of X-ray-selected AGNs observed at $4 < z < 6$ aligns well with the prediction of this hypothesis, as shown by the green curve indicating AGNs that undergo their second episodes. This agreement further supports the idea that LRDs represent the earliest phase of AGN activity, after which the objects evolve into normal AGNs.

In the right panel of Figure 2, we show the fraction of AGNs that have experienced their second or later episodes relative to the total AGN population, representing the fraction of non-LRDs under this hypothesis. Since a significant fraction of BHs undergo a second episode at $z < 5$, this fraction increases rapidly and reaches unity by $z \sim 3$. For comparison, we overlay observational constraints on the fraction of unobscured (non-LRD) AGNs (95% confidence level), derived from a sample of 62 spectroscopically confirmed broad-line AGNs in the redshift range of $3.5 < z < 6$ (A. J. Taylor et al. 2025a). At $z \leqslant 6$, the sample size in each redshift bin is sufficiently large to reveal a trend that closely follows the model prediction (black curve).[4] The redshift range where LRDs begin to diminish coincides with the emergence of typical unobscured AGNs.

The emergence conditions of LRDs are likely tied to the underlying BH seeding mechanisms and the surrounding environment. One proposed model is the heavy seed scenario, in which seed BHs form through the direct collapse of massive atomic gas clouds (e.g., A. Loeb & F. A. Rasio 1994; V. Bromm & A. Loeb 2003; M. C. Begelman et al. 2006; C. Shang et al. 2010, see also K. Inayoshi et al. 2020). Alternatively, the lack of an obvious host galaxy component in LRDs (C.-H. Chen et al. 2025) implies that processes beyond baryonic physics might be involved. For instance, the collapse

of a halo core via energy dissipation in a self-interacting dark matter environment has been proposed (e.g., W.-X. Feng et al. 2021; M. Grant Roberts et al. 2025; F. Jiang et al. 2025). In both scenarios, a key prediction is that BH formation precedes active star formation and yields a BH-to-stellar mass ratio substantially higher than the local empirical value (e.g., H. Hu et al. 2025; F. Jiang et al. 2025). Notably, a recently reported LRD with its broad Hβ emission at $z_{\rm spec} = 9.288$, CAPERS-LRD-z9, shows an apparent overmassiveness in the ratio (A. J. Taylor et al. 2025b), offering an opportunity for testing the BH seeding channel along with the transitional trend of LRD abundance relative to the entire BH population (see the right panel of Figure 2). Moreover, the initial accretion episodes onto newly born seed BHs are likely led by intense cold flows along cosmic filaments in overdense regions of the Universe (T. Di Matteo et al. 2012) and may occur through gas with low angular momentum (D. J. Eisenstein & A. Loeb 1995). The timing of these accretion processes, potentially influenced by the spin distribution of the halo, may be crucial for the emergence of LRDs (see also P. Kroupa et al. 2020).

The physical origin of the log-normal occurrence distribution for LRDs (and more broadly, AGN activity) remains an open question. However, the observed statistical properties suggest that the occurrence time, $t_{\rm AGN}$, is determined by the product of multiple independent physical quantities x_i ($i = 1, 2, \cdots n$) with some inherent randomness, such that

$$t_{\rm AGN} = x_1 x_2 \cdots x_n. \tag{4}$$

If the logarithms of these variables, $\log x_i$, follow distributions that satisfy weak conditions, the central limit theorem implies that the distribution of $\log t_{\rm AGN}$ tends toward a normal distribution as n increases. In astrophysical contexts, while $n \to \infty$ is not strictly applicable, even a modest number ($n \sim 3$) is sufficient to produce a log-normal distribution (e.g., K. Ioka & T. Nakamura 2002). This statistical (i.e., *macroscopic*) property can be described without specifying the detailed *microscopic* physical processes that govern AGN triggering. Modeling the specific mechanisms that set the mean

---

[4] Since the sample size at $6 < z < 7$ is too small for robust statistical analysis (one LRD and three unobscured AGNs), we do not include the data in the right panel of Figure 2. Statistical uncertainties are evaluated using the Clopper–Pearson method.

and variance of the distribution will be left for future studies (e.g., BH coalescences via gravitational-wave emission; K. Inayoshi et al. 2025).
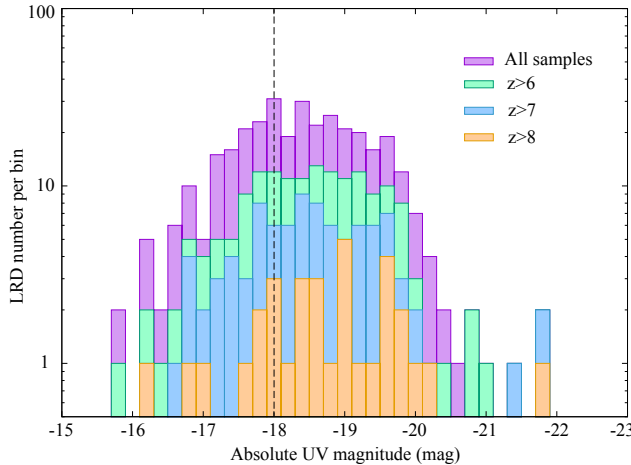
Appendix A
Selection

The left panel of Figure 3 shows the distribution of LRD detections as a function of absolute UV magnitude with the total sample (purple) and subsets at $z \geqslant 6$ (green), $z \geqslant 7$ (blue), and $z \geqslant 8$ (orange). The histogram peaks at $M_{\rm UV} \sim -18$ mag with a decline on both the brighter and fainter sides. The rarity of LRDs on the brighter end suggests an intrinsically lower abundance, while the decline on the fainter end is likely due to flux limits, as also seen in the UV luminosity functions at $M_{\rm UV} > -18$ mag (D. D. Kocevski et al. 2025). The characteristic bending magnitude remains consistent across all redshift bins.

The right panel of Figure 3 presents the LRD occurrence rate for each UV-magnitude bin, along with the best-fit log-normal distribution (solid curves). The fitted parameters, summarized in Table 1, fall within the 1σ uncertainty range. Even when considering only bright LRDs with $M_{\rm UV} < -18$ mag, the emergence trend of LRDs at

Table 1
Fitting Results with a Log-normal Distribution

	t_0 (Myr)	σ_0
All sample	865 ± 20	0.297 ± 0.0184
$M_{\rm UV} < -18$	850 ± 19	0.278 ± 0.0167
$M_{\rm UV} < -19$	808 ± 27	0.288 ± 0.0258

$t \gtrsim 0.5$ Gyr remains robust. Thus, we conclude that this trend reflects an intrinsic phenomenon rather than a selection effect.

Appendix B
Diminishing LRD Features Due to Mergers with Other Galaxies

One possible explanation for the decline in the LRD occurrence rate at $z < 4$–5 is that their unique features, especially their compact morphology (e.g., D. D. Kocevski et al. 2025; I. Labbe et al. 2025), are lost due to mergers with normal galaxies. Major mergers could cause LRDs to appear as extended sources, blending stellar components with the underlying AGN and diminishing their LRD-like characteristics. Indeed, dual LRD candidates with $\sim$1–2 kpc projected separations have been reported (T. S. Tanaka et al. 2024). Cosmological N-body simulations estimate that major mergers (with a mass ratio of $\xi \gtrsim 0.3$) occur with a frequency of $p \sim 0.2$ per halo per redshift interval (O. Fakhouri et al. 2010). This suggests that the number of LRDs that avoid such mergers and retain their unique features decreases toward lower redshifts as

$$\frac{dN_{\rm LRD}}{dz} \simeq N_0 e^{-p(z_0 - z)}. \quad (B1)$$

Figure 4 presents two curves representing $dN_{\rm LRD}/dt$ for $p = 0.2$ (cyan) and $p = 0.5$ (blue), where N_0 is adjusted to match the histogram at a cosmic age of $\sim$1 Gyr. The case with $p = 0.2$ approximately corresponds to a scenario where the comoving number density of LRDs follows a power-law evolution, $\phi \propto t^{-1}$, consistent with the overall cosmic evolution of the number density of galaxies over $0 < z < 8$ (C. J. Conselice et al. 2016). Even in an extreme case where
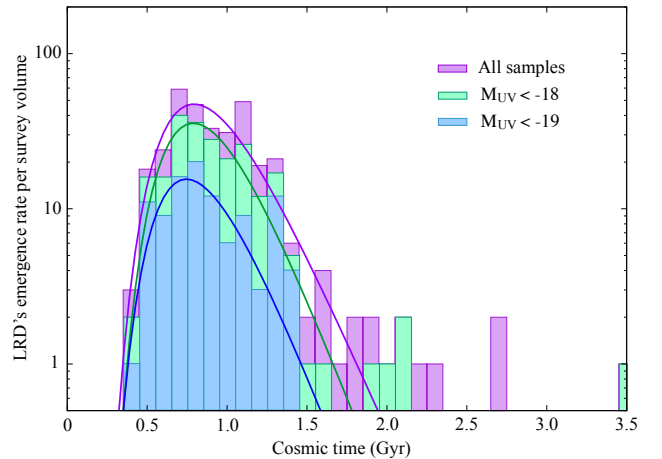

Figure 3. Left: the distribution of UV absolute magnitudes for LRDs with the total sample (purple) and subsets at $z \geqslant 6$ (green), $z \geqslant 7$ (blue), and $z \geqslant 8$ (orange). The vertical line indicates a reference threshold of $M_{\rm UV} = -18$ mag, fainter than which the observed decline in number is likely due to flux limits. Right: the LRD occurrence rate for the total sample (purple) and subsets at $M_{\rm UV} < -18$ (green) and $M_{\rm UV} < -19$ (blue) overlaid with best-fit log-normal distributions (solid curves).
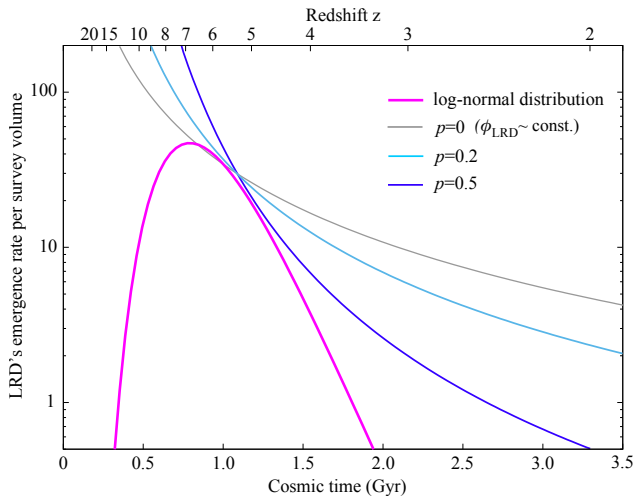
Figure 4. The LRD occurrence-rate models: the log-normal case (magenta) and the decay cases driven by mergers: $p = 0$ (gray), $p = 0.2$ (cyan), and $p = 0.5$ (blue).

$p = 0.5$ (implying that 50% of LRDs undergo merger in each redshift interval, a rate observed in simulations for minor mergers), the resulting decline trend is still significantly shallower than the log-normal decay (magenta curve). This suggests that mergers alone cannot fully account for the rapid disappearance of LRDs at lower redshifts, unless minor mergers with $\xi \gtrsim 0.03$ would diminish LRD characteristics.

In addition, it is worth noting that the mass growth of LRD host galaxies through subsequent halo and galaxy mergers is likely a key driver of their evolution toward other galaxy populations. In particular, gas-rich mergers can trigger intense starbursts while maintaining compact morphologies (L. Oser et al. 2010), potentially transforming LRDs into "red nuggets" by intermediate redshifts—systems considered to be the progenitors of present-day giant elliptical galaxies (D. Thomas et al. 2005; I. Trujillo et al. 2009). An intriguing property of an LRD has been reported by V. Kokorev et al. (2024b), which exhibits a spectrum dominated by evolved stellar populations with a mass of $M_\star \sim 10^{10.6} M_\odot$ and no signs of ongoing star formation. Other studies have similarly identified massive quiescent galaxies at high redshifts (e.g., A. C. Carnall et al. 2023; M. Onoue et al. 2024; B. Wang et al. 2024; A. de Graaff et al. 2025), whose cosmic abundance approaches the upper limit predicted by the flat ΛCDM cosmology (e.g., A. C. Carnall et al. 2024), as observed for LRD populations under an assumption that all observed light originates from stellar populations (H. B. Akins et al. 2024; K. Inayoshi & K. Ichikawa 2024; B. Wang et al. 2024). Importantly, the detection of broad Hα emission lines in some of these quiescent galaxies suggests that their star formation was quenched by AGN activity a few hundred million years prior to the observed epoch. Future work will clarify the evolutionary connection between LRDs and their descendants at lower redshifts, as well as the transition from LRDs to more typical AGN populations.

Appendix C
Analytic Formula

When the occurrence times of AGN events are independently and identically distributed, the central limit theorem states that the cumulative occurrence time until the nth AGN event will approximately follow a Gaussian distribution with mean $n\mu$ and variance $n\sigma^2$, where μ and σ^2 are the mean and variance of the occurrence time distribution for each single event. Although the occurrence timing follows a log-normal distribution, for simplicity, we approximate it as a Gaussian distribution with mean μ and variance σ^2. This assumption allows for an analytical treatment for the calculation of the cosmic AGN occurrence rate. The total occurrence rate at a given cosmic time t is expressed as

$$\frac{dN_{\rm AGN}}{dt} = \sum_{k=1}^{n} \frac{N_0}{\sqrt{2\pi}\,\sigma_i} e^{-(t-\mu_k)^2/2\sigma_k^2}, \quad \text{(C1)}$$

where $\mu_k = k\mu$ and $\sigma_k = \sqrt{k}\,\sigma$ for $1 \leqslant k \leqslant n$. For sufficiently large $k \gtrsim k_0 \equiv (\mu/\sigma)^2$, the dispersion σ_k becomes large enough that the separation between each Gaussian peak becomes smaller than the dispersion, and thus each Gaussian distribution largely overlaps. Therefore, at later times of $t > k_0\mu = \mu^3/\sigma^2$, the sum can be approximated by an integral form and evaluated using the saddle-point method around $x = t/\mu$,

$$\frac{dN_{\rm AGN}}{dt} = \frac{N_0}{\sqrt{2\pi}\,\sigma} \int_0^\infty \exp\left[\frac{-(t-\mu x)^2}{2\sigma^2 x}\right] \frac{dx}{x} \simeq \frac{N_0}{\mu}. \quad \text{(C2)}$$

The result turns out *time-independent*. This trend is consistent with the numerical result of $\phi \propto (1 + z)^{-5/2}$ shown in Figure 2, and aligns with measurements of AGN abundances in the range $0 < z < 5$ (Y. Ueda et al. 2014) as well.

ORCID iDs

Kohei Inayoshi ⓘ https://orcid.org/0000-0001-9840-4959

References

Akins, H. B., Casey, C. M., Lambrides, E., et al. 2024, arXiv:2406.10341
Begelman, M. C., Volonteri, M., & Rees, M. J. 2006, MNRAS, 370, 289
Bromm, V., & Loeb, A. 2003, ApJ, 596, 34
Carnall, A. C., Cullen, F., McLure, R. J., et al. 2024, MNRAS, 534, 325
Carnall, A. C., McLure, R. J., Dunlop, J. S., et al. 2023, Natur, 619, 716
Chen, C.-H., Ho, L. C., Li, R., & Zhuang, M.-Y. 2025, ApJ, 983, 60
Conselice, C. J., Wilkinson, A., Duncan, K., & Mortlock, A. 2016, ApJ, 830, 83
de Graaff, A., Setton, D. J., Brammer, G., et al. 2025, NatAs, 9, 280
Delvecchio, I., Gruppioni, C., Pozzi, F., et al. 2014, MNRAS, 439, 2736
Di Matteo, T., Khandai, N., DeGraf, C., et al. 2012, ApJL, 745, L29
Eisenstein, D. J., & Loeb, A. 1995, ApJ, 443, 11
Ellsworth, W. L., Matthews, M. V., Nadeau, R. M., et al. 1999, A Physically-based Earthquake Recurrence Model for Estimation of Long-term Earthquake Probabilities, Tech. Rep. 99-522, US Geological Survey
Fakhouri, O., Ma, C.-P., & Boylan-Kolchin, M. 2010, MNRAS, 406, 2267
Feng, W.-X., Yu, H.-B., & Zhong, Y.-M. 2021, ApJL, 914, L26
Grant Roberts, M., Braff, L., Garg, A., et al. 2025, JCAP, 2025, 060
Greene, J. E., Labbe, I., Goulding, A. D., et al. 2024, ApJ, 964, 39
Hainline, K. N., Maiolino, R., Juodžbalis, I., et al. 2025, ApJ, 979, 138
Harikane, Y., Zhang, Y., Nakajima, K., et al. 2023, ApJ, 959, 39
Hu, H., Inayoshi, K., Haiman, Z., et al. 2022, ApJ, 935, 140
Hu, H., Inayoshi, K., Haiman, Z., Ho, L. C., & Ohsuga, K. 2025, ApJL, 983, L37
Inayoshi, K., & Ichikawa, K. 2024, ApJL, 973, L49
Inayoshi, K., Kimura, S., & Noda, H. 2024, arXiv:2412.03653
Inayoshi, K., Nakatani, R., Toyouchi, D., et al. 2022, ApJ, 927, 237
Inayoshi, K., Shangguan, J., Chen, X., Ho, L. C., & Haiman, Z. 2025, arXiv:2505.05322
Inayoshi, K., Visbal, E., & Haiman, Z. 2020, ARA&A, 58, 27
Ioka, K., & Nakamura, T. 2002, ApJL, 570, L21
Ji, X., Maiolino, R., Übler, H., et al. 2025, arXiv:2501.13082
Jiang, F., Jia, Z., Zheng, H., et al. 2025, arXiv:2503.23710
Juodžbalis, I., Ji, X., Maiolino, R., et al. 2024, MNRAS, 535, 853

Khan, F. M., Davis, B. L., Macciò, A. V., & Holley-Bockelmann, K. 2025, ApJL, 986, L1

Kirsten, F., Ould-Boukattine, O. S., Herrmann, W., et al. 2024, NatAs, 8, 337

Kocevski, D. D., Finkelstein, S. L., Barro, G., et al. 2025, ApJ, 986, 126

Kocevski, D. D., Onoue, M., Inayoshi, K., et al. 2023, ApJL, 954, L4

Kokorev, V., Caputi, K. I., Greene, J. E., et al. 2024a, ApJ, 968, 38

Kokorev, V., Chisholm, J., Endsley, R., et al. 2024b, ApJ, 975, 178

Kormendy, J., & Ho, L. C. 2013, ARA&A, 51, 511

Kroupa, P., Subr, L., Jerabkova, T., & Wang, L. 2020, MNRAS, 498, 5652

Labbe, I., Greene, J. E., Bezanson, R., et al. 2025, ApJ, 978, 92

Li, H., & Fenimore, E. E. 1996, ApJL, 469, L115

Li, W., Inayoshi, K., Onoue, M., & Toyouchi, D. 2023, ApJ, 950, 85

Li, W., Inayoshi, K., & Qiu, Y. 2021, ApJ, 917, 60

Loeb, A., & Rasio, F. A. 1994, ApJ, 432, 52

Ma, Y., Greene, J. E., Setton, D. J., et al. 2025, arXiv:2504.08032

Madau, P., & Haardt, F. 2024, ApJL, 976, L24

Maiolino, R., Risaliti, G., Signorini, M., et al. 2025, MNRAS, 538, 1921

Maiolino, R., Scholtz, J., Curtis-Lake, E., et al. 2024, A&A, 691, A145

Matthee, J., Naidu, R. P., Brammer, G., et al. 2024, ApJ, 963, 129

Onoue, M., Ding, X., Silverman, J. D., et al. 2024, arXiv:2409.07113

Onoue, M., Inayoshi, K., Ding, X., et al. 2023, ApJL, 942, L17

Oser, L., Ostriker, J. P., Naab, T., Johansson, P. H., & Burkert, A. 2010, ApJ, 725, 2312

Pérez-González, P. G., Barro, G., Rieke, G. H., et al. 2024, ApJ, 968, 4

Planck Collaboration, Ade, P. A. R., Aghanim, N., et al. 2016, A&A, 594, A13

Pouliasis, E., Ruiz, A., Georgantopoulos, I., et al. 2024, A&A, 685, A97

Reines, A. E., & Volonteri, M. 2015, ApJ, 813, 82

Scoggins, M. T., & Haiman, Z. 2024, MNRAS, 531, 4584

Shang, C., Bryan, G. L., & Haiman, Z. 2010, MNRAS, 402, 1249

Tanaka, T. S., Silverman, J. D., Shimasaku, K., et al. 2024, arXiv:2412.14246

Taylor, A. J., Finkelstein, S. L., Kocevski, D. D., et al. 2025a, ApJ, 986, 165

Taylor, A. J., Kokorev, V., Kocevski, D. D., et al. 2025b, arXiv:2505.04609

Thomas, D., Maraston, C., Bender, R., & de Oliveira, C. M. 2005, ApJ, 621, 673

Trinca, A., Schneider, R., Valiante, R., et al. 2022, MNRAS, 511, 616

Trujillo, I., Cenarro, A. J., de Lorenzo-Cáceres, A., et al. 2009, ApJL, 692, L118

Ueda, Y., Akiyama, M., Hasinger, G., Miyaji, T., & Watson, M. G. 2014, ApJ, 786, 104

Valiante, R., Schneider, R., Volonteri, M., & Omukai, K. 2016, MNRAS, 457, 3356

Volonteri, M., Habouzit, M., & Colpi, M. 2021, NatRP, 3, 732

Wang, B., de Graaff, A., Davies, R. L., et al. 2025, ApJ, 984, 121

Wang, B., Leja, J., de Graaff, A., et al. 2024, ApJL, 969, L13